

Texture Based Superpixel Segmentation Algorithm for Hyperspectral Image Classification

Subhashree Subudhi

International Institute of Information Technology

Ramnarayan Patro

International Institute of Information Technology

Pradyut Kumar Biswal (✉ pradyut@iiit-bh.ac.in)

International Institute of Information Technology

Research Article

Keywords: Hyperspectral Image Classification, Superpixel Segmentation, SLIC, Spatial-Spectral Feature Extraction

Posted Date: June 10th, 2022

DOI: <https://doi.org/10.21203/rs.3.rs-1721548/v1>

License: © ⓘ This work is licensed under a Creative Commons Attribution 4.0 International License.

[Read Full License](#)

Texture Based Superpixel Segmentation Algorithm for Hyperspectral Image Classification

Subhashree Subudhi¹, Ramnarayan Patro¹ and Pradyut
Kumar Biswal^{1*}

^{1*}Department of Electronics and Telecommunication,
International Institute of Information Technology, Street,
Bhubaneswar, 751003, Odisha, India.

*Corresponding author(s). E-mail(s): pradyut@iiit-bh.ac.in;
Contributing authors: ssubudhi84@gmail.com;
ram_patro@rediffmail.com;

Abstract

Superpixel segmentation is a potential preprocessing tool that can simplify an image by creating semantic sub-regions of the image. This is quite effective in reducing the misclassification of isolated pixels. Image segmentation using superpixels has been successfully applied in the computer vision field. Recently, superpixel segmentation is being adopted into HSI processing domain also, due to its superior properties. In this work, for the accurate classification of the Hyperspectral Image, a texture-based superpixel segmentation algorithm is proposed. Local Binary Pattern (LBP) and Gabor filters are first incorporated to extract the local and global image texture information. Next, Simple Linear Iterative Clustering (SLIC) superpixel segmentation algorithm is applied over the extracted texture features and a superpixel segmentation map is obtained. Finally, majority voting strategy is performed between the superpixel segmentation map and the pixel-wise classification map to acquire the final classification map. For validating the effectiveness of the proposed algorithm, experiments were conducted on four popular HSI datasets, namely: Indian Pines, Pavia University, Houston 2013, and Houston 2018 datasets. Superior classification performance was observed by the proposed method in comparison to other state-of-the-art methods.

Keywords: Hyperspectral Image Classification, Superpixel Segmentation, SLIC, Spatial-Spectral Feature Extraction

1 Introduction

In applications such as urban planning, ecology, precision farming, defense, mining, and space explorations, accurate classification of remote sensing images is a very crucial task. With recent advancements in the hyperspectral imaging system, now for each spatial location in the image, it is possible to record the electromagnetic spectrum in various narrow contiguous spectral bands. In addition, small spatial structures in the image can also be analyzed by Hyperspectral (HS) sensors of very high spatial resolution. However, there are several challenges involved in the classification of Hyperspectral Image (HSI). It suffers from the Hughes effect or curse of dimensionality as it has a limited proportion of reference samples over hundreds of spectral bands. Also, there exists high spatial variability of spectral signatures. Many hyperspectral image classification techniques have been developed, which only exploits the rich spectral information of HSI, and neglects the spatial details. Some of the popular traditional classification methods are , maximum likelihood, neural network, k -nearest neighbors, logistic regression and support vector machine (SVM). But, the classification performance by using only spectral features is not at all encouraging because of the large spectral variability produced by materials properties and environmental factors. In HSI, significant improvement in the classification performance can be achieved by considering the homogeneous spatial distribution of surface materials. Therefore, in recent years more emphasis is laid on the spatial-spectral feature extraction step and some of such approaches are discussed further. Mathematical Morphology based approaches are extensively applied by researchers for Feature Extraction (FE). Benediktsson et al.[1] first introduced the concept of Extended Morphological Profiles (EMP) for FE in HSI. It utilizes morphological closing and opening operations to extract spatial features. Later, Dalla Mura et al. [2] proposed Morphological Attribute Filters (MAP) for the spatial FE. From that point onwards, several variations of Attribute Profiles (AP) were created. Ghamisi et al. [3] conducted a comprehensive survey on the evolution in Attribute Profile. Texture Descriptors like Wavelet transform [4], Gray-Level Co-occurrence Matrix (GLCM) [5], Local Binary Patterns (LBP) [6] and Gabor filters [7] are also used in literature for spatial FE.

The filters that are usually incorporated for noise removal can also be utilized for spatial-spectral FE [8]. The spatial distribution of neighborhood pixels is of greater significance in the filtration process as it carries crucial edge information. Hence, several edge-preserving filters like Domain Transform Recursive Filters [9], Bilateral Filters [10], Guidance filters [11], Trilateral Filters [12] etc. were introduced. For minimization of noise and texture variations, smoothening operations are performed by these filters. Along with that, they

also preserve the most crucial attributes like lines, edges, and other features that help in image interpretation.

Segmentation is another popular approach for inclusion of spatial features [13]. With the traditional fixed window-based methods, the occurrence of salt and pepper noise in the classification result is quite prevalent. Also, it is difficult to adaptively capture the information regarding the changing shape and size of the structural object. To deal with the above challenges, the concept of superpixel segmentation has emerged as a new option recently [14]. It creates smaller meaningful patches that can adhere to the object boundaries by grouping pixels that have homogeneous properties. As superpixels reduce the redundancy and complexity in the image, the performance of the subsequent processing steps can be enhanced significantly. Hence, superpixels can be employed to compute the local image features. Due to the numerous advantages of superpixels, they are now widely used for effective feature extraction in HSI as well. In [15], the authors concentrated on the various ways in which established superpixel techniques might be employed as a preprocessing step for HSI analysis, with a particular focus on classification. There are no dedicated superpixel segmentation algorithms specifically designed for HSI. The segmentation algorithms which are primarily designed for natural RGB images are also utilized for analysing HSI data. But as HS images contain rich amount of information it is not advisable to apply superpixel segmentation directly on raw HSI. The quality of generated superpixel map greatly depends on the base image [15] on which the algorithms are applied. Hence, in this work the SLIC superpixel segmentation algorithm is applied on the feature space rather than the PCA image in order to accurately extract the contextual features in the image.

In this paper, texture-based superpixel segmentation algorithms are proposed for HSI classification. Extracting useful information from HSI is quite challenging. Hence, Gabor and LBP features are first applied on HSI image, to highlight the key discriminant features. Further, the popular Simple Linear Iterative Clustering (SLIC) algorithm is applied on the extracted texture features to acquire more enhanced features which aids in the classification process. The final classification map is regularized with the help of the generated superpixel segmentation map by using the majority voting strategy. The obtained result clearly reveals the superiority of the proposed LBP-SLIC method against other state-of-the-art algorithms.

The major contributions of the proposed approach are highlighted below:

- A novel approach for integration of SLIC superpixel segmentation with the texture descriptors such as LBP and Gabor is presented.
- A modified SLIC algorithm with the following changes are made.
 - SLIC is applied on high dimensional texture features to get more highlighted spatial structural information.
 - Hexagonal grid is defined for cluster initialization so that spatial groups with improved homogeneity can be obtained.

- A new distance measure is incorporated as here SLIC is applied on the texture features.

The manuscript is organized as follows: A concise description of various superpixel segmentation algorithms is discussed in Section 3. Next, the proposed work is explained in Section 4. The experimental results are presented in Section 5. Finally, the conclusion is provided in Section 6.

2 Introduction

In applications such as urban planning, ecology, precision farming, defense, mining, and space explorations, accurate classification of remote sensing images is a very crucial task. With recent advancements in the hyperspectral imaging system, now for each spatial location in the image, it is possible to record the electromagnetic spectrum in various narrow contiguous spectral bands. In addition, small spatial structures in the image can also be analyzed by Hyperspectral (HS) sensors of very high spatial resolution. However, there are several challenges involved in the classification of Hyperspectral Image (HSI). It suffers from the Hughes effect or curse of dimensionality as it has a limited proportion of reference samples over hundreds of spectral bands. Also, there exists high spatial variability of spectral signatures. Many hyperspectral image classification techniques have been developed, which only exploits the rich spectral information of HSI, and neglects the spatial details. Some of the popular traditional classification methods are , maximum likelihood, neural network, k -nearest neighbors, logistic regression and support vector machine (SVM). But, the classification performance by using only spectral features is not at all encouraging because of the large spectral variability produced by materials properties and environmental factors. In HSI, significant improvement in the classification performance can be achieved by considering the homogeneous spatial distribution of surface materials. Therefore, in recent years more emphasis is laid on the spatial-spectral feature extraction step and some of such approaches are discussed further. Mathematical Morphology based approaches are extensively applied by researchers for Feature Extraction (FE). Benediktsson et al. [1] first introduced the concept of Extended Morphological Profiles (EMP) for FE in HSI. It utilizes morphological closing and opening operations to extract spatial features. Later, Dalla Mura et al. [2] proposed Morphological Attribute Filters (MAP) for the spatial FE. From that point onwards, several variations of Attribute Profiles (AP) were created. Ghamisi et al. [3] conducted a comprehensive survey on the evolution in Attribute Profile. Texture Descriptors like Wavelet transform [4], Gray-Level Co-occurrence Matrix (GLCM) [5], Local Binary Patterns (LBP) [6] and Gabor filters [7] are also used in literature for spatial FE.

The filters that are usually incorporated for noise removal can also be utilized for spatial-spectral FE [8]. The spatial distribution of neighborhood pixels is of greater significance in the filtration process as it carries crucial edge information. Hence, several edge-preserving filters like Domain Transform

Recursive Filters [9], Bilateral Filters [10], Guidance filters [11], Trilateral Filters [12] etc. were introduced. For minimization of noise and texture variations, smoothing operations are performed by these filters. Along with that, they also preserve the most crucial attributes like lines, edges, and other features that help in image interpretation.

Segmentation is another popular approach for inclusion of spatial features [13]. With the traditional fixed window-based methods, the occurrence of salt and pepper noise in the classification result is quite prevalent. Also, it is difficult to adaptively capture the information regarding the changing shape and size of the structural object. To deal with the above challenges, the concept of superpixel segmentation has emerged as a new option recently [14]. It creates smaller meaningful patches that can adhere to the object boundaries by grouping pixels that have homogeneous properties. As superpixels reduce the redundancy and complexity in the image, the performance of the subsequent processing steps can be enhanced significantly. Hence, superpixels can be employed to compute the local image features. Due to the numerous advantages of superpixels, they are now widely used for effective feature extraction in HSI as well. In [15], the authors concentrated on the various ways in which established superpixel techniques might be employed as a preprocessing step for HSI analysis, with a particular focus on classification. There are no dedicated superpixel segmentation algorithms specifically designed for HSI. The segmentation algorithms which are primarily designed for natural RGB images are also utilized for analysing HSI data. But as HS images contain rich amount of information it is not advisable to apply superpixel segmentation directly on raw HSI. The quality of generated superpixel map greatly depends on the base image [15] on which the algorithms are applied. Hence, in this work the SLIC superpixel segmentation algorithm is applied on the feature space rather than the PCA image in order to accurately extract the contextual features in the image.

In this paper, texture-based superpixel segmentation algorithms are proposed for HSI classification. Extracting useful information from HSI is quite challenging. Hence, Gabor and LBP features are first applied on HSI image, to highlight the key discriminant features. Further, the popular Simple Linear Iterative Clustering (SLIC) algorithm is applied on the extracted texture features to acquire more enhanced features which aids in the classification process. The final classification map is regularized with the help of the generated superpixel segmentation map by using the majority voting strategy. The obtained result clearly reveals the superiority of the proposed LBP-SLIC method against other state-of-the-art algorithms.

The major contributions of the proposed approach are highlighted below:

- A novel approach for integration of SLIC superpixel segmentation with the texture descriptors such as LBP and Gabor is presented.
- A modified SLIC algorithm with the following changes are made.

- SLIC is applied on high dimensional texture features to get more highlighted spatial structural information.
- Hexagonal grid is defined for cluster initialization so that spatial groups with improved homogeneity can be obtained.
- A new distance measure is incorporated as here SLIC is applied on the texture features.

The manuscript is organized as follows: A concise description of various superpixel segmentation algorithms is discussed in Section 3. Next, the proposed work is explained in Section 4. The experimental results are presented in Section 5. Finally, the conclusion is provided in Section 6.

3 Related Work

Superpixels which serve as a precursor to image segmentation task, can be described as an unsupervised oversegmentation of an image into several semantic sub-regions, bearing similar characteristic features. This concept was initially introduced in the year 2003 by Ren and Malik [16]. Using superpixels for segmentation has several advantages: (1) Features can be computed on more meaningful regions instead of acting on individual pixels. (2) Computational complexity reduces drastically as the input entries for subsequent algorithms reduce significantly. A superpixel must have certain desirable properties as described by Machairas et al. [17]. They are:

- **Homogeneity:** The generated superpixels must have uniform pixel values.
- **Boundary Adherence:** Superpixel boundaries must match the object boundaries.
- **Regularity:** Superpixels must be placed in a regular pattern in the image.
- **Time Complexity:** The generated superpixels should have lower computational complexity and higher efficiency.
- **Connected Partition:** Superpixels consist of a connected set of pixels and the overlapping of superpixels must not exist.

In the area of computer vision, the concept of superpixel segmentation has already gained a lot of popularity due to the aforementioned properties of superpixels. In such applications segmentation is mostly performed over the color and grayscale images. A detailed survey on the state-of-the-art superpixel segmentation algorithms for color images is provided by Stutz et al. [14]. The author has broadly categorized the superpixel algorithms into seven categories: Density-based, Watershed-based, Graph-based, Path-based, Contour Evolution-based, Energy Optimization-based and Clustering-based approaches.

Recently superpixel segmentation algorithms have been incorporated for HSI classification, as it can very well represent the spatial regularity of the surface materials in HSI. These segmentation algorithms partition the HS image into several homogeneous sub-regions, thereby reducing the computational complexity in the subsequent image processing tasks drastically. In [15],

a comprehensive review of superpixel segmentation methods for HSI classification is presented. The article also analyzed different superpixel creation algorithms and post-processing frameworks for using superpixels in HSI. Chen et al. [18] proposed a spatial-spectral classification framework where superpixel segmentation and pixel-wise classification results are merged using a fuzzy-logic combination rule. Segmentation can be used to improve the classification results of SVM classifier by applying majority voting inside each segment [19]. A superpixel-based Markov random field model for HSI classification was presented by Li et al [20]. Later, Fang et al. [21] adopted superpixels to exploit spatial-spectral information via multiple kernels. A multiscale superpixel-level subspace-based SVM for HSI classification was then proposed by Yu et.al [22]. The pixel correlation within each superpixel was also considered by Tu et al. [23] in order to exploit spatial-spectral features. Liu et.al [24] developed a multi-morphological superpixel model in for HS image classification. In remote sensing community, Entropy Rate Superpixels (ERS) [23] and SLIC [24], algorithms are vastly applied for superpixel segmentation. This is mainly because both these algorithms are faster and they can generate compact superpixels which adhere well with the object boundaries[25]. Watershed segmentation algorithm was applied by Zhang et al.[26] on a fused gradient image generated from multispectral bands. This helps in overcoming the oversegmentation problem in watershed segmentation.

4 Proposed Method

The authors in [15] have mentioned the different ways in which superpixel algorithms can be applied as a preprocessing step for HSI analysis along with the pros and cons of each of the approaches. Hence, by taking the motivation from that article, in this paper we decided to incorporate SLIC on the feature space to create superpixels. Superpixel segmentation when applied on the feature space, generates enhanced spatial structure and reduces the incorrect boundary regions [24]. The framework for superpixel generation is presented in Fig. 1. In most of the existing approaches, SLIC is applied on the composite image of first three PCA bands as the reduced image becomes similar to the natural RGB image hence, the SLIC algorithm originally developed for general images can be applied easily. But by reducing the dimension of HSI, significant amount of information is lost. So, to extract enhanced spatial structures and correct boundary information, feature extractors like LBP and Gabor can be applied on the PCA image. In the first approach, Gabor filter is applied on the PCA image to extract the global texture information. The extracted gabor features is then provided as an input to SLIC for segmentation map generation. In the second approach, to effectively capture the local texture information LBP is applied over the PCA image and the resultant features is fed as an input to SLIC for superpixel map generation. The framework for the validation of the proposed superpixel generation method is presented in Fig. 2. A pixel-wise classification map is first produced by directly employing the SVM classifier

on the initial HSI image. The derived spatial information from the superpixel segmentation map is next incorporated in spatial-spectral classification by employing the majority voting strategy [27]. This technique is mostly used here to regularize/optimize the classification map with the guidance of the segmentation map. It is based on the assumption that an unlabeled pixel, after initial classification, that has the same class label of neighboring pixels, is reliable. Fig. 3, shows an illustrative example of the combination of spectral and spatial information using the majority voting classification method. A detailed explanation of the modified SLIC algorithm and the texture descriptors used in this work is presented in the below subsection.

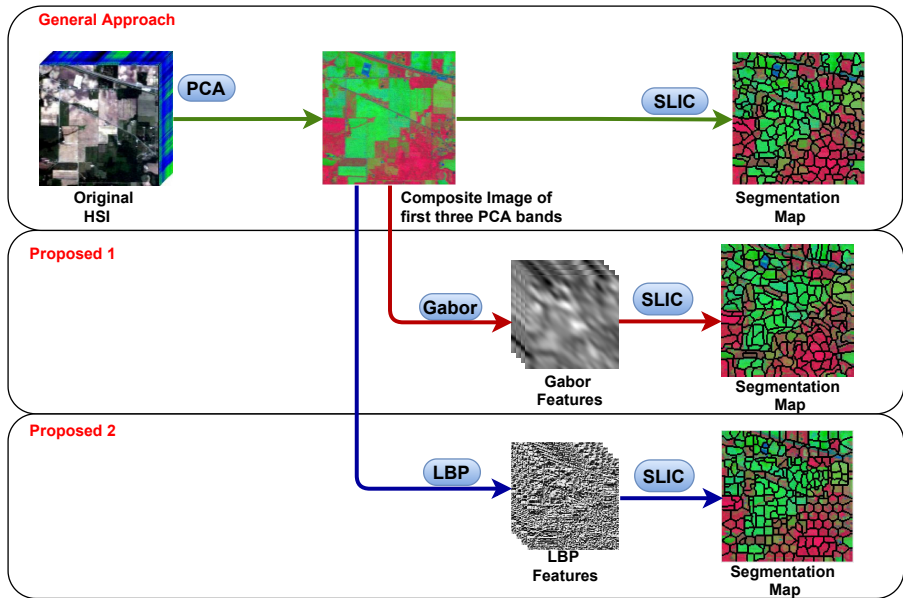


Fig. 1 Proposed framework for superpixel generation

4.1 SLIC algorithm

SLIC [28] algorithm is the most widely used method for grouping set of similar pixels into a region. It is a popular gradient-ascent-based superpixel segmentation approaches, where an initially defined tentative set of cluster points are iteratively refined using a gradient-ascent method until some convergence criteria are met. This algorithm has lower computational complexity as it applies the k -means method locally. The algorithm includes four key steps: Cluster center initialization, Cluster assignment, Cluster center updation, and post-processing. In this work, a modified SLIC algorithm with the following changes is presented so as to obtain improved segmentation results: (1) Hexagonal grids

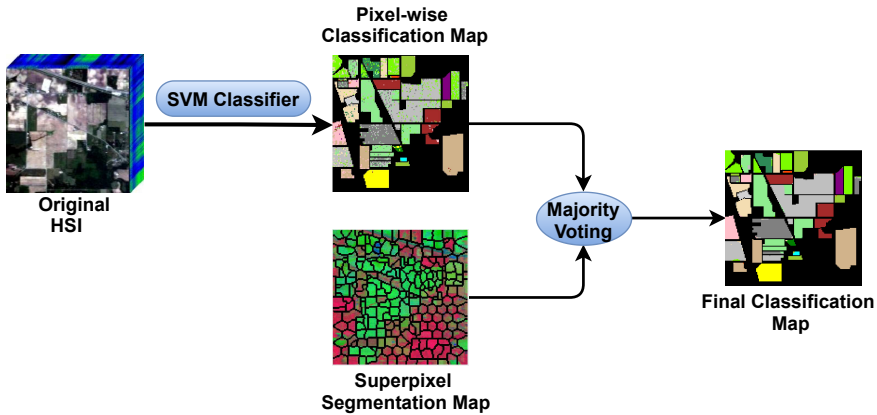


Fig. 2 Validation of the proposed approach

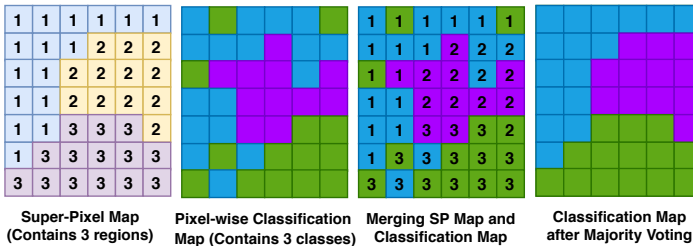


Fig. 3 Majority Voting Strategy

for cluster center initialization, (2) Application of SLIC on texture features, and (3) Incorporation of a new distance measure. Each of these changes are explained in details in below section.

To generate initial clusters, the standard SLIC algorithm uses a square grid. But, in the proposed method hexagonal grids are defined for cluster center initialization. Fig. 4 contains the architecture of the basic hexagonal grid structure where each corner and each edge are shared by three and two hexagons respectively. There are two main advantages of using hexagonal grids over square grids: (1) More number of off-diagonal neighbors are available for each hexagon hence, the surrounding spatial information can be learned more accurately and (2) less distance distortion of boundary pixels is provided by hexagonal grids. Hence, with the modified SLIC algorithm, spatial groups with improved homogeneity can be obtained. Fig. 4 contains the structure of a basic hexagonal grid. To describe the hexagon's size height h and width w is computed. To represent the spacing between the adjacent hexagons vertical distance V and horizontal distance T is used. The center of the hexagon can

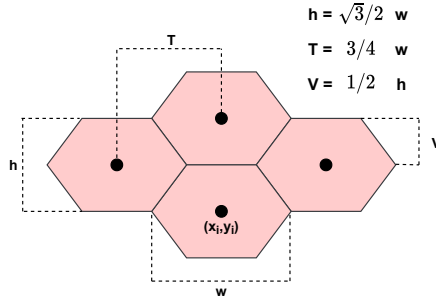


Fig. 4 Hexagonal grid structure

be calculated using the following simple matrix multiplication (Eqn.1).

$$\begin{bmatrix} x_i \\ y_i \end{bmatrix} = \begin{bmatrix} T & 0 \\ V & h \end{bmatrix} \begin{bmatrix} r_i \\ c_i \end{bmatrix} \quad (1)$$

where $[x_i, y_i]$ represents the i^{th} cluster center's spatial coordinates. $[r_i, c_i]$ are the row and column indices of the i^{th} superpixel. The segmentation process is initialized in accordance with the width and height of the hexagon. The central pixel coordinates are used as the initial coordinates and the origin is at the upper left corner of the image. The average spectrum is based on the spectrum of the centre pixel. Even though, the superpixel's spatial extent is assumed to be a hexagonal region, the search operation is performed on a region of size $2U \times 2U$ around the superpixel in order to find similar pixels. Hence, with regard to the number of pixels, the computational complexity is still linear.

The original SLIC algorithm was developed for natural images having red, green and blue channels. But in case of HSI, it is not advisable to directly apply SLIC as the red, green and blue channels are not covered by some HSIs. To overcome this problem, often the initial three Principal Components (PC's) are utilized to create pseudocolor images [29]. But several issues still exist. The underlying significant spectral information of HSI can not be explored completely by the SLIC as after applying PCA, the image dimension is reduced drastically. The SLIC algorithm is modified in this paper, so that it can utilize the key discriminative features of all the spectral bands along with the spatial information of the surface material to produce the superpixel segmentation map. But superpixel segmentation when applied directly on the raw HSI may result in over-segmentation. To overcome this problem in this paper, superpixel segmentation is performed on the extracted texture features. This in turn results in more highlighted spatial structural information, thereby minimizing the influence of faulty region boundaries, decreasing disparity within the same class, and inhibiting over-segmentation. The quality of the generated superpixels greatly depends upon the features over which it is applied. In this paper two popular texture descriptors: LBP and Gabor filters are employed to derive local and global image texture information. Highly distinguished surface

materials can be obtained by these texture descriptors. Let the extracted texture features are represented as $\mathbf{F} = \{\mathbf{f}_1, \mathbf{f}_2, \dots, \mathbf{f}_N\} \in \mathbb{R}^{B \times N}$ with N pixels and B number of feature band. Each pixel can be represented as $\mathbf{A}_i = [\mathbf{f}_i, \mathbf{x}_i, \mathbf{y}_i]^T$ where, $\mathbf{f}_i^T = [\mathbf{f}_1, \mathbf{f}_2, \dots, \mathbf{f}_B]^T$ is the feature vector and $[\mathbf{x}_i, \mathbf{y}_i]^T$ is the position vector. The K number of initial cluster centers $\mathbf{C}_j = [\mathbf{f}_j, \mathbf{x}_j, \mathbf{y}_j]^T$ are sampled on a regular hexagonal grid and are thus equally spaced apart.

After initialization of cluster centers, the next step is the cluster assignment step, where each pixel is assigned to the nearby cluster center based on the computed distance measure D . Distance is computed within a $2U \times 2U$ window around the cluster center. The distance between the cluster center C_j and pixel A_i is calculated as follows (Eqn. 2):

$$D = D_{feature} + \frac{W}{U} D_{spatial} \quad (2)$$

where, W is the weighting factor between spectral and spatial features. Note that the distance is identical to one in the original SLIC algorithm. The only modification is new definition of $D_{feature}$. In this paper, as we are applying SLIC on the texture features, the color space is getting changed. Hence, there is a need to update the corresponding spectral distance measure to Spectral Information Divergence (SID) [30]. SID is one of the most popular measure to compute spectral similarity between two pixels by measuring the discrepancy between them. The dissimilarity measure among the pair of feature vectors can be represented as in Eqn. 3:

$$D_{feature} = \sum_{i,j=1}^N f_i \log(f_i/f_j) + \sum_{i,j=1}^N f_j \log(f_j/f_i) \quad (3)$$

where, $D_{feature}$ is the measure of homogeneity within the superpixels. f_i and f_j are the features vectors at pixel i and j respectively.

The spatial distance between feature vectors A_i and A_j are represented as in Eqn. 4

$$D_{spatial} = \sqrt{(x_i - x_j)^2 + (y_i - y_j)^2} \quad (4)$$

where, (x, y) denotes the location of pixel i in superpixel. The spatial distance $D_{spatial}$ ensures regularity and compactness in the generated superpixels.

The cluster assignment step is next followed by the cluster center updation step. Here, the superpixel center coordinates and the center spectrum are updated. The center coordinates takes the average coordinates of all pixels in the superpixel and the center spectrum takes average spectrum of all pixels in the superpixel. The cluster assignment and updation steps are iteratively repeated until convergence criterion is met.

In the final step, post-processing is performed to enforce connectivity by reassigning disjoint pixels to nearby superpixels.

4.2 Texture Descriptors

4.2.1 Gabor

Gabor filter is a widely used texture feature extractor and edge detector [7]. It is basically generated by multiplying a Gaussian Kernel with a sinusoidal wave. Mathematical representation of a 2-dimensional Gabor filter is as follows:

$$G_{\lambda,\theta,\varphi,\sigma,\gamma}(m,n) = \exp\left(\frac{-m'^2 + \gamma^2 n'^2}{2\sigma^2}\right) \exp\left(j\left(2\pi\frac{m'}{\lambda} + \varphi\right)\right) \quad (5)$$

where,

$$m' = m\cos\theta + n\sin\theta \quad (6)$$

$$n' = -m\sin\theta + n\cos\theta \quad (7)$$

where λ represents the sinusoidal factor wavelength, θ specifies the Gabor kernel's orientation, φ is the phase shift, σ represents the Gaussian kernel's standard deviation and γ denotes the Gabor function's spatial aspect ratio. The Gabor filter's real and the imaginary parts are returned by $\varphi = 0$ and $\varphi = \pi/2$ respectively. The standard deviation σ is determined with the help of λ and spatial frequency bandwidth BW as

$$\sigma = \frac{\lambda}{\pi} \sqrt{\frac{\ln(2)}{2} \frac{2^{BW} + 1}{2^{BW} - 1}} \quad (8)$$

The Gabor Features are extracted by applying the Gabor filter on the pseudocolor image of first three PCA bands (Fig. 1). These extracted texture features are further used for performing the superpixel segmentation.

4.2.2 Local Binary Pattern

Another popular texture descriptor is a Local Binary Pattern (LBP) which can effectively summarize the local structures in an image. The computation of LBP involves two key steps: Encoding each point in a block as a pattern and gathering statistics of LBP occurrences in the form of a histogram. For the first step, LBP operator is applied on a texture unit. A texture unit is a basic element for LBP encoding. Figure. 5 illustrates the encoding process. For the center pixel g_c , its local neighborhood g_i is a set of evenly spaced sampling points P located in a circle of radius R (Fig.5). If the pixel value g_i of the neighboring pixels is greater than the center pixel, it is assigned a value 1, otherwise 0. The LBP code can be mathematically represented as:

$$LBP_{P,R}(g_c) = \sum_{i=0}^{P-1} t(g_i - g_c) 2^i \quad (9)$$

$$t(z) = \begin{cases} 1, & z \geq 0 \\ 0, & z < 0 \end{cases} \quad (10)$$

Hence, the generated LBP code for g_c is 189. However, the range of LBP code varies from 0 to 255, which have several disadvantages. The 256-level LBP is

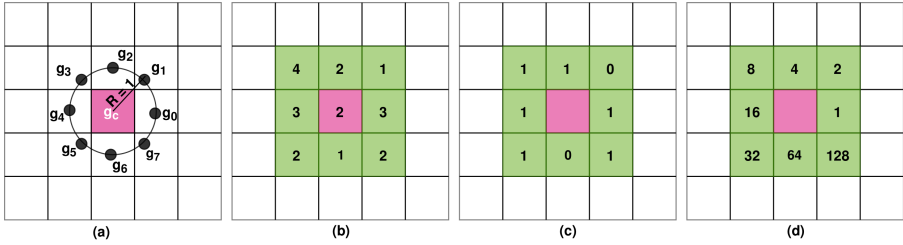


Fig. 5 (a) Texture Unit with radius $r = 1$, center pixel g_c and its neighbors g_i (b) Sample 3×3 block (c) Binary labels for neighboring points (d) Weights

ineffective in case of noisy images. Also, the time and space complexity of the feature extraction procedure increases drastically as the feature dimension is $256 \times B$, where B represents the available spectral bands. The stability of the generated LBP code is also not good enough. Hence, in order to resolve the aforementioned problems, an uniform LBP (ULBP) code is utilized for texture feature extraction [31]. In ULBP, if the number of bitwise transitions ($0 \rightarrow 1$ or $1 \rightarrow 0$) is less than or equal to 2, it is considered as an uniform sample and is assigned with a unique index (from 0 to 57). In case of more than two transitions, an index 58 is assigned. The mathematical formulation for ULBP is as follows:

$$LBP_{P,R}(g_c) = \begin{cases} \sum_{i=0}^{P-1} t(g_i - g_c), & \text{if } U(LBP_{P,R}(g_c)) \leq 2 \\ [P(P-1) + 3] - 1, & \text{Otherwise} \end{cases} \quad (11)$$

where,

$$U(LBP_{P,R}(g_c)) = t(g_{P-1} - g_c) + \sum_{i=1}^{P-1} t(g_i - g_c) - t(g_{i-1} - g_c) \quad (12)$$

Finally, after obtaining the LBP code, the LBP occurrence statistics is gathered in the form of a histogram.

In this work, ULBP is applied on the PCA reduced HSI in order to extract LBP codes. Then, ULBP histogram is computed for each pixel in an image patch around a pixel, in order to construct ULBP features of each principal component in HSI. The extracted ULBP features are displayed in Fig. 1. Finally, the extracted LBP texture features serve as a base image upon which superpixel segmentation is applied.

5 Experimental Result

5.1 Experimental Data

To experimentally validate the performance of the proposed method, four popular datasets namely Indian Pines, Pavia University, Houston 2013, and

Houston 2018 were utilized. These datasets have different characteristic behavior in terms of spectral and spatial resolution. The basic information regarding the datasets is presented in a tabular form in Table. 1.

Table 1 Dataset description

Dataset	Spectral Range (nm)	Total Bands	Reduced Band	Image Size (pixels)	Classes	Spatial Resolution (m/pixels)
Indian Pines	400-2500	224	200	145 x 145	16	20
Pavia University	430-860	115	103	610 x 340	9	1.3
Houston 2013	380-1050	144	144	349 x 1905	15	2.5
Houston 2018	380-1050	50	50	601 x 2384	20	1

In Fig. 6, 7, 8, and 9 the false-color composite image, ground truth image, and class names for Indian Pines, Pavia University, Houston 2013, and Houston 2018 datasets respectively are provided.

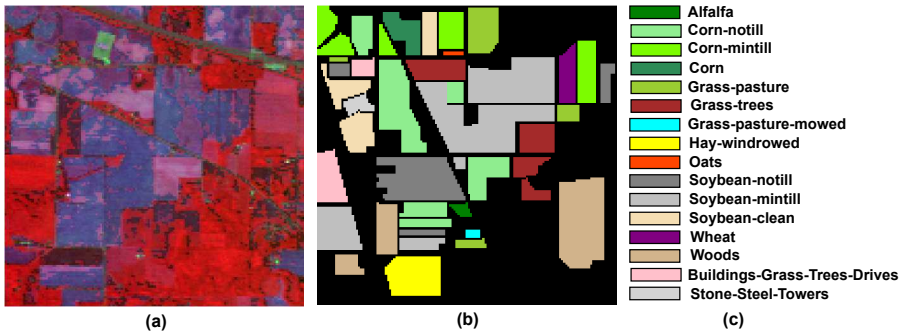


Fig. 6 (a) False-color Composite Image, (b) Ground Truth Image and (c) Class names for Indian Pines Dataset

5.2 Experimental Setup

To validate the effectiveness of the proposed superpixel algorithm, it is compared with other state-of-the-art algorithms like SVM [32], EMP [1], Edge Preserving Filter (EPF) [33], Simple Linear Iterative Clustering (SLIC) [28], Superpixel-based Classification via Multiple Kernels (SCMK) [21], Superpixelwise PCA (SuperPCA) [34], Adjacent superpixel-based Generalized Spatial-Spectral Kernel (ASGSSK) [35], Convolutional Neural Network-Pixel Pair Features (CNN-PPF) [36], and 3D-CNN [37]. For training, 3%, 2%, and 0.2% of samples were randomly selected from each class for the Indian Pines, Pavia University, and Houston 2018 datasets respectively. In the case of the Houston 2013 dataset, 30 samples were chosen randomly for training. All the experiments were independently repeated for 10 iterations with different train/test sets to generate results that are statistically more remarkable,

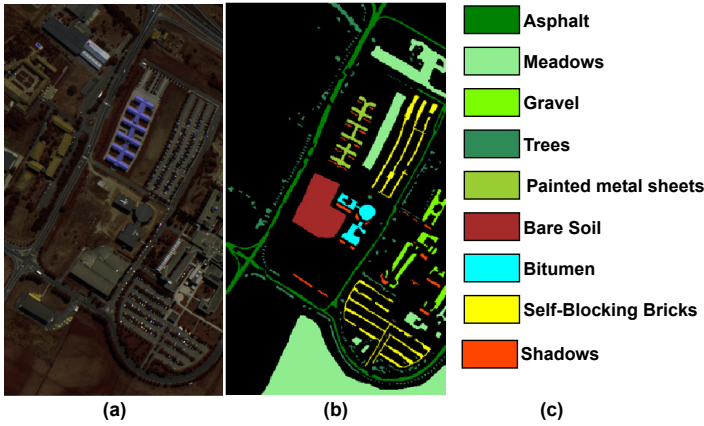


Fig. 7 (a) False-Color Composite Image, (b) Ground Truth Image and (c) Class names for Pavia University Dataset

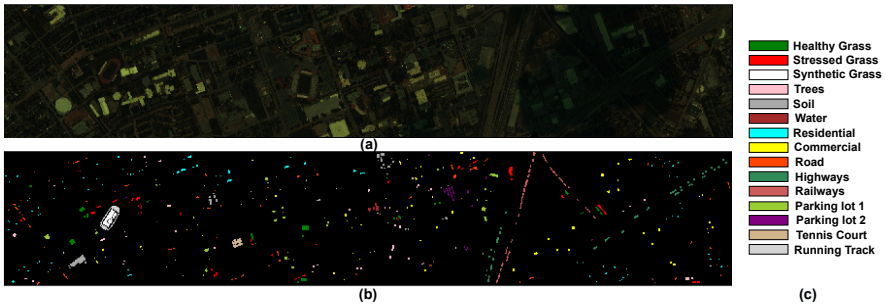


Fig. 8 (a) False-Color Composite Image, (b) Ground Truth Image and (c) Class names for Houston-2013 Dataset

and the mean classification accuracy along with standard deviation values are finally reported. With random train/test split, the systematic errors and random discrepancies can be avoided easily and unbiased results can be produced.

The performance of different algorithms are evaluated by using five popular performance metrics i.e., Overall Accuracy (OA), Average Accuracy(AA), Kappa Coefficient, class-by-class accuracy, and computation time. All the experiments were performed using MATLAB R2018b software, installed on a computer having Intel core i5-6200 CPU 2.30GHz and 16 GB RAM.

The SVM classifier adopts a one-vs-one multi-class approach for classification. The LIBSVM package was utilized for the implementation of SVM. The regularization parameter C and RBF kernel parameter γ are determined by using a five-fold cross-validation approach. To obtain a fair comparison

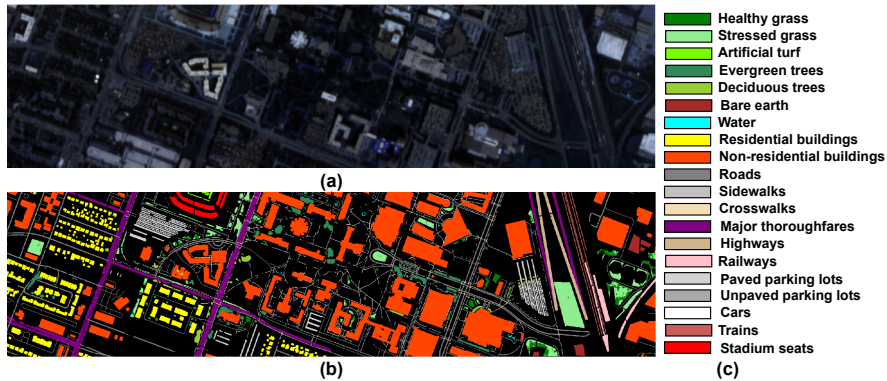


Fig. 9 (a) False-Color Composite Image, (b) Ground Truth Image and (c) Class names for Houston-2018 Dataset

for the EMP, EPF, SLIC, SC-MK, SuperPCA, ASGSSK, CNN-PPF, and 3D-CNN methods the default parameter settings provided in the corresponding publications were utilized.

The value of parameter K has a significant influence on the classification performance. Depending on the structural and texture information available in the dataset, the value of K must be decided. In Figure. 10(b), a plot is shown to demonstrate the effect of the number of superpixels K on the classification accuracy for the proposed method when K is varied from 100 to 1600. In the proposed work, the value of K is taken as 300 for the Indian Pines dataset as it contains a large portion of homogeneous regions. Hence, a lower value of K is preferred. Whereas for the Pavia University, Houston 2013, and Houston 2018 datasets, a larger value of K i.e. 1000 is chosen as these datasets contain more detailed structural and texture information. Hence, there is a need to devote a higher number of superpixels to effectively capture the available information.

In LBP-SLIC and Gabor-SLIC, texture features are first extracted using ULBP and Gabor filters respectively. For ULBP, the considered parameters are: radius (R) is taken as 1 with 8 evenly spaced sampling points P . The block size of 21×21 is used to compute the LBP. Figure. 10(a), contains a plot showing the effect of variation in block size on the classification accuracy. It can be observed that variation in block size has not much influence on the classification accuracy for the four experimented datasets. Hence, we may use any block size. For all the test cases, a block size of 25×25 is considered for evaluation. Whereas for the Gabor filter the bandwidth BW was taken as 1 for the Indian Pines dataset. But for the Pavia University, Houston 2013, and Houston 2018 datasets BW was considered to be 5. The value of wavelength λ was chosen as 16. As a result, eight orientations i.e. $[0, \pi/8, \pi/4, 3\pi/8, \pi/2, 5\pi/8, 3\pi/4, 7\pi/8]$ were considered. The default value for the Gabor function's aspect ratio was selected as 0.5.

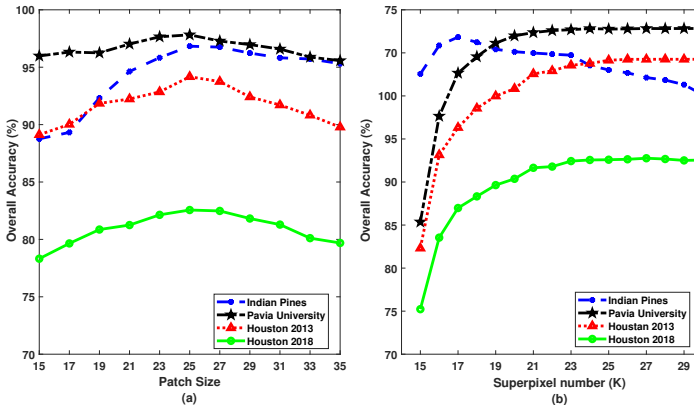


Fig. 10 (a) Effect of block size on the classification accuracy for proposed LBP-SLIC method (b) Effect of number of superpixels K on the classification accuracy for the proposed LBP-SLIC method

5.3 Result and Discussion

The quantitative and qualitative performance of the proposed method along with the other nine compared approaches are provided in this section, using four popular HSI datasets.

Initially, the effect of training sample variation on the classification performance for different methods is analyzed in Figure 11. The experiment was conducted on the four datasets i.e. Indian Pines, Pavia University, Houston 2013, and Houston 2018 datasets. From Figure 11, it can be observed that the increment in the number of training samples has a positive influence on the classification performance.

In Tables 2-5, the classification accuracies for the four datasets are provided to evaluate the performance of the proposed method quantitatively. Also, the classification maps for the proposed method along with the other compared methods on the four different datasets are presented in Figures. 12-15 respectively.

5.3.1 Indian Pines

The classification result with 3 % training samples from each class is provided in Table 2. It can be noted that for the proposed LBP-SLIC method, superior classification accuracy is obtained for most of the classes. In comparison to the SVM method, an improvement of about 17.32 % and 15.82% in OA is obtained with the proposed LBP-SLIC and Gabor-SLIC methods respectively. In general the superpixel-based methods, mainly produce improved classification results as the local spatial information is effectively captured using the

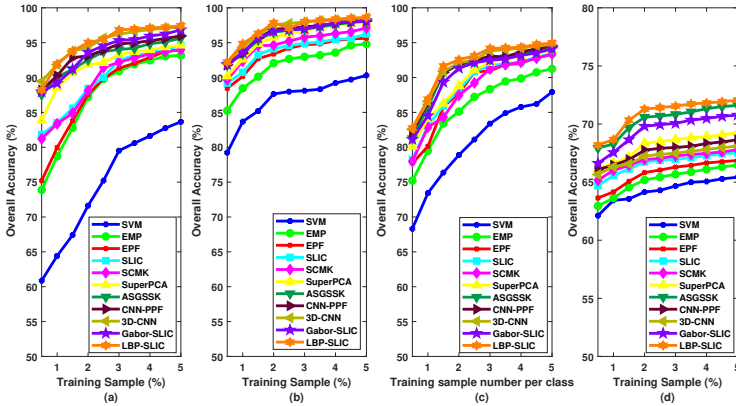


Fig. 11 Effect of training sample variation on classification performance for (a) Indian Pines (b) Pavia University (c) Houston 2013 datasets, and (d) Houston 2018 dataset

superpixels. The proposed approach even outperforms the deep learning methods (3D-CNN and CNN-PPF) as these techniques generally demand more training samples.

As observed in Figure, 12 when the spectral features are only considered, a very noisy map is obtained for the SVM method. But with the incorporation of spatial features, a much smoother classification map is generated for the EMP and EPF methods. However, in the detailed and edge regions, these approaches fail to accurately classify the pixels. Meanwhile, for the compared superpixel-based methods (SLIC, SCMK, SuperPCA, and ASGSSK) improved performance is obtained. The proposed LBP-SLIC and Gabor-SLIC algorithms show superior or comparable performance as compared to the other existing superpixel classification algorithms. Mainly the proposed LBP-SLIC method shows superior performance as compared to other approaches. This happens mainly due to the inclusion of the LBP features into the SLIC algorithm. The proposed algorithm utilizes the LBP features to capture the local texture information for the creation of superpixel segments. In Gabor-SLIC, Gabor features are utilized for extracting the global texture information which is in-turn utilized for performing superpixel segmentation.

5.3.2 Pavia University

In Table 3, the classification result with 2% training samples from each class is provided and the corresponding classification map is displayed in Figure. 13. In this case also, the classification map for SVM is still very noisy. Whereas, for EMP and EPF methods, comparatively much smoother maps are obtained with less salt and pepper noise. The amount of misclassification further reduces with the incorporation of superpixel-based methods. It can be clearly noticed from Table. 3, that the proposed LBP-SLIC approach still produces the best performance in comparison to all other experimented methods.

Table 2 Classification Result for Indian Pines Dataset with 3% training samples from each class for SVM, EMP, EPF, SLIC, SCMK, SuperPCA, ASGSSK, CNN-PPF, 3D-CNN, Gabor-SLIC, and LBP-SLIC algorithms. Number in the parentheses denote the standard deviation of the accuracies obtained in repeated experiments.

Class	Samples	SVM [32]	EMP [1]	EPF [33]	SLIC [28]	SCMK [21]	SuperPCA [34]	ASGSSK [35]	CNN-PPF [36]	3D-CNN [37]	Gabor-SLIC	LBP-SLIC
1	46	63.89(4.29)	65.12(3.45)	81.41(1.96)	95.35(1.28)	97.67(0.91)	87.81(4.23)	97.44(0.58)	86.05(1.49)	92.86(3.27)	82.93(2.83)	89.19(5.21)
2	1428	72.97(6.82)	83.31(2.62)	86.96(2.13)	84.34(1.72)	91.09(3.64)	90.51(2.76)	92.82(1.18)	89.05(3.22)	91.01(2.43)	91.01(2.63)	93.87(1.75)
3	830	78.27(7.03)	91.79(2.21)	90.26(3.45)	94.56(2.37)	95.02(1.58)	94.65(1.27)	97.62(0.85)	95.55(1.66)	90.96(4.58)	95.62(1.83)	98.34(0.65)
4	237	46.56(10.33)	86.04(4.12)	98.65(2.15)	90.00(3.05)	97.25(1.69)	92.86(2.24)	96.57(0.94)	89.95(3.31)	92.2(2.86)	95.69(0.67)	90.48(3.42)
5	483	95.85(1.53)	88.99(3.43)	89.87(2.13)	95.10(0.48)	90.11(2.37)	94.94(0.88)	97.34(0.76)	97.30(2.54)	95.96(2.31)	96.95(0.45)	96.11(0.77)
6	730	97.44(2.55)	99.27(0.21)	99.42(0.32)	98.08(0.59)	96.73(1.24)	97.87(1.53)	98.89(0.98)	99.85(0.23)	97.02(1.18)	99.07(0.12)	98.63(0.84)
7	28	75.45(3.42)	84.62(2.13)	99.48(0.16)	85.19(3.48)	100.00(0.00)	100.00(0.00)	100.00(0.00)	98.68(1.21)	99.94(0.01)	87.50(3.54)	100.00(0.00)
8	478	98.69(1.34)	98.89(2.21)	100.00(0.00)	94.16(2.78)	99.54(0.27)	99.53(0.31)	99.03(0.11)	99.77(0.18)	95.91(2.67)	99.29(0.38)	100.00(0.00)
9	20	62.51(1.32)	100.00(0.00)	84.21(4.56)	57.89(6.71)	55.56(6.74)	94.44(2.13)	100.00(0.00)	68.42(8.94)	78.95(6.82)	94.12(4.21)	93.75(3.87)
10	972	78.12(4.61)	88.51(2.34)	88.51(1.86)	93.24(1.81)	93.97(0.97)	90.63(3.75)	96.77(0.64)	93.85(3.57)	93.92(1.83)	96.66(0.63)	
11	2455	68.398(3.31)	93.07(3.44)	91.63(2.94)	94.92(1.37)	93.14(2.12)	94.30(1.62)	96.10(0.88)	93.36(2.31)	89.96(4.82)	95.05(1.62)	96.59(0.86)
12	593	75.95(6.81)	80.65(3.31)	73.84(3.86)	73.37(4.82)	78.90(2.27)	93.81(3.51)	89.61(2.83)	88.81(4.73)	86.97(3.21)	90.60(3.11)	94.73(0.88)
13	205	98.79(0.84)	91.19(2.54)	96.89(1.93)	90.05(2.74)	89.42(3.41)	100.00(0.00)	96.61(0.75)	88.30(5.22)	95.24(2.71)	91.71(2.56)	95.12(2.12)
14	1265	93.08(1.64)	97.31(1.37)	96.30(2.21)	96.51(1.81)	97.08(0.87)	98.68(0.65)	98.34(0.34)	98.02(1.96)	96.13(2.27)	99.73(0.05)	99.80(0.11)
15	386	71.73(5.37)	90.08(2.31)	98.90(2.57)	97.49(3.24)	97.46(2.84)	99.71(0.21)	99.40(0.14)	98.03(1.77)	95.49(2.59)	98.82(0.35)	99.68(0.13)
16	93	93.33(2.11)	95.45(1.65)	77.01(3.57)	95.40(1.32)	91.86(2.31)	96.39(1.22)	81.01(3.15)	97.67(2.69)	84.88(7.35)	95.06(1.53)	94.59(2.11)
OA ::		79.51(1.21)	90.92(0.66)	91.35(1.21)	92.19(0.75)	93.30(1.50)	94.82(1.12)	96.20(0.79)	94.01(0.68)	92.52(1.02)	95.33(0.61)	96.83(0.86)
AA ::		75.88(1.34)	89.65(1.12)	90.86(0.86)	89.73(1.52)	91.55(0.87)	92.51(0.68)	96.13(0.51)	92.62(1.35)	92.33(0.86)	94.19(1.05)	96.10(0.51)
Kappa ::		74.81(0.64)	89.66(0.81)	90.14(0.58)	91.11(0.88)	92.36(0.21)	94.10(0.39)	95.67(0.72)	93.17(1.02)	91.49(0.75)	94.68(0.82)	96.38(0.61)
Time (sec) ::		5.65	16.82	11.34	10.51	13.22	15.37	18.54	265.46	210.34	42.35	54.81

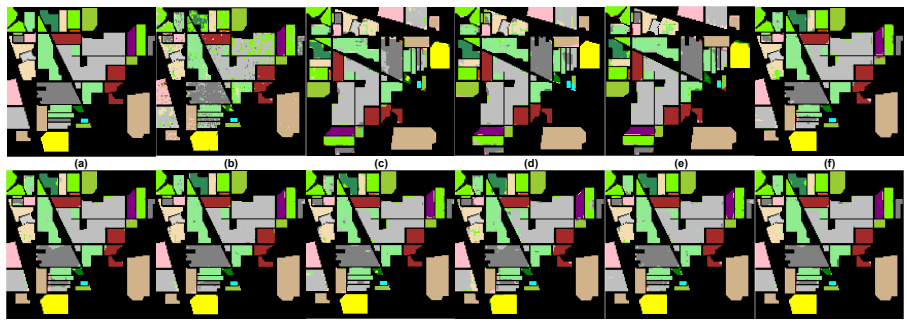


Fig. 12 (a) Ground Truth Image, Classification Maps of (b) SVM (c) EMP (d) EPF (e) SLIC (f) SCMK (g) SuperPCA (h) ASGSSK (i) CNN-PPF (j) 3D-CNN (k) Gabor-SLIC (l) LBP-SLIC for Indian Pines dataset

An improvement of about 10.18 % and 9 % in OA is obtained using LBP-SLIC and Gabor-SLIC methods respectively in comparison to the baseline SVM approach. The ASGSSK algorithm also produces almost similar results like LBP-SLIC.

Table 3 Classification Result for Pavia University Dataset with 2% training samples from each class for SVM, EMP, EPF, SLIC, SCMK, SuperPCA, ASGSSK, CNN-PPF, 3D-CNN, Gabor-SLIC, and LBP-SLIC algorithms. Number in the parentheses denote the standard deviation of the accuracies obtained in repeated experiments.

Class	Samples	SVM [32]	EMP [1]	EPF [33]	SLIC [28]	SCMK [21]	SuperPCA [34]	ASGSSK [35]	CNN-PPF [36]	3D-CNN [37]	Gabor-SLIC	LBP-SLIC
1	6631	88.16(3.57)	89.94(4.28)	95.69(0.67)	93.18(1.59)	96.43(1.72)	97.23(1.12)	97.29(0.47)	96.05(1.06)	94.35(2.24)	94.55(1.22)	96.29(0.65)
2	18649	94.74(4.71)	97.29(1.08)	96.57(1.17)	99.27(0.03)	99.80(0.14)	99.61(0.17)	99.77(0.08)	98.50(1.24)	97.62(1.56)	99.81(0.08)	99.73(0.05)
3	2099	69.4(3.79)	75.7(5.58)	74.39(3.64)	78.7(2.44)	81.09(1.65)	87.41(0.98)	88.46(1.24)	86.81(4.35)	85.41(3.17)	92.76(0.24)	87.49(1.51)
4	3064	86.37(2.87)	78.49(1.54)	89.59(1.43)	92.82(0.87)	88.99(1.05)	95.07(1.14)	96.97(0.98)	94.13(2.31)	92.84(3.14)	94.54(0.87)	95.55(1.08)
5	1345	99.72(0.05)	96.19(1.27)	95.12(2.31)	99.92(0.02)	98.12(0.88)	97.51(1.19)	97.32(1.21)	98.50(8.62)	98.56(1.36)	98.25(1.67)	99.89(0.04)
6	5029	68.76(6.64)	92.78(2.41)	90.91(3.47)	92.81(0.87)	95.11(1.34)	96.25(1.27)	97.66(0.89)	93.55(1.42)	91.73(2.94)	96.96(1.61)	98.30(2.55)
7	1330	82.33(4.24)	93.72(2.81)	89.23(3.14)	78.55(3.84)	94.38(1.31)	97.39(0.76)	96.05(0.64)	97.49(2.67)	94.62(2.73)	89.03(2.88)	94.91(0.83)
8	3692	82.28(3.71)	87.54(3.89)	90.22(2.79)	90.34(2.51)	91.74(1.45)	91.96(0.97)	93.42(0.72)	91.41(1.34)	83.73(3.68)	91.66(1.64)	94.62(0.64)
9	447	99.87(0.02)	90.01(1.56)	95.21(2.24)	97.71(2.23)	96.38(0.87)	90.2(2.31)	96.95(0.52)	93.28(1.88)	94.05(2.34)	96.66(0.75)	96.59(0.53)
OA ::		87.64(1.07)	92.07(0.67)	93.88(1.08)	94.66(0.72)	95.78(0.59)	97.58(0.27)	97.58(0.27)	95.93(1.21)	94.14(1.35)	96.64(0.63)	97.82(0.62)
AA ::		85.74(1.26)	89.07(1.01)	90.84(1.13)	91.46(0.64)	93.52(0.51)	94.73(0.26)	95.99(0.12)	94.42(1.18)	92.55(1.24)	94.74(0.81)	96.19(0.47)
Kappa ::		83.47(0.92)	89.66(1.05)	91.23(0.69)	92.80(0.58)	94.39(0.45)	95.91(0.68)	96.79(0.71)	94.61(1.32)	92.24(1.91)	95.54(0.73)	97.10(0.56)
Time (sec) ::		9.5	33.69	21.57	20.68	25.67	23.52	36.21	298.21	369.45	98.34	87.62

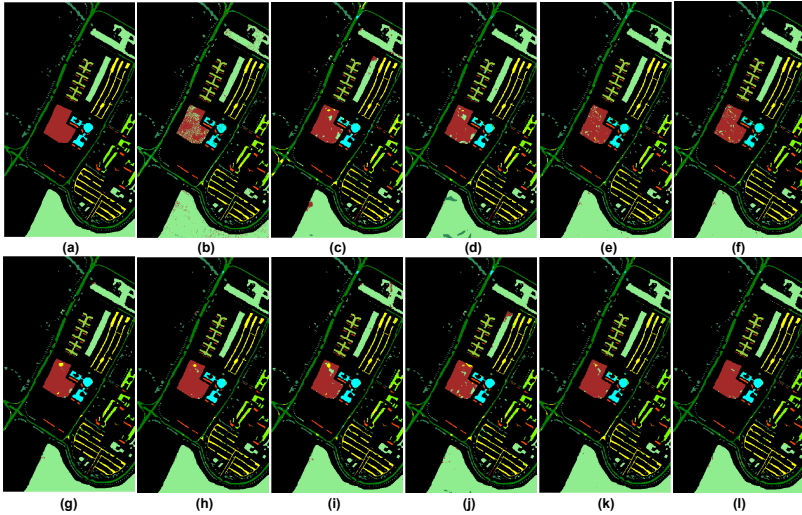


Fig. 13 (a) Ground Truth Image, Classification Maps of (b) SVM (c) EMP (d) EPF (e) SLIC (f) SCM (g) SuperPCA (h) ASGSSK (i) CNN-PPF (j) 3D-CNN (k) Gabor-SLIC (l) LBP-SLIC for Pavia University dataset

5.3.3 Houston 2013

To evaluate the performance of the investigated approaches, 30 labeled samples from each class were selected as training samples. In Table 4, the classification results are presented. A visual comparison of different methods performance is displayed in Figure. 14. From Table 4, it can be clearly observed that the proposed LBP-SLIC method outperforms all the compared methods in terms of OA, AA, and Kappa. Also, the classification map closely resembles the Ground Truth image for the proposed method.

Table 4 Classification Result for Houston 2013 Dataset with 30 training samples from each class for SVM, EMP, EPF, SLIC, SCM, SuperPCA, ASGSSK, CNN-PPF, 3D-CNN, Gabor-SLIC, and LBP-SLIC algorithms. Number in the parentheses denote the standard deviation of the accuracies obtained in repeated experiments.

Class	Samples	SVM [32]	EMP [1]	EPF [33]	SLIC [28]	SCMK [21]	SuperPCA [34]	ASGSSK [35]	CNN-PPF [36]	3D-CNN [37]	Gabor-SLIC	LBP-SLIC
1	1251	83.17(10.21)	97.16(2.65)	94.84(3.62)	97.13(1.84)	91.65(4.51)	96.44(1.46)	98.76(1.28)	99.43(0.65)	96.67(2.94)	97.93(2.12)	96.97(1.05)
2	1254	94.75(4.63)	96.27(2.21)	97.63(1.86)	94.85(5.52)	97.88(1.36)	95.21(2.13)	95.78(3.21)	96.73(1.44)	96.35(2.34)	94.13(3.08)	99.17(0.81)
3	697	93.84(5.81)	99.41(0.21)	98.35(1.25)	98.95(1.11)	100.00(0.00)	98.93(1.05)	100.00(0.00)	98.20(0.85)	98.76(0.29)	99.23(0.37)	99.07(0.21)
4	1244	87.06(3.87)	94.44(4.27)	93.41(3.29)	96.13(1.74)	95.47(2.57)	96.34(3.81)	95.9(3.95)	93.33(4.21)	97.91(3.18)	98.25(2.51)	96.82(3.73)
5	1242	100.00(0.00)	97.3(2.44)	96.62(2.85)	97.69(3.12)	99.92(0.02)	96.75(1.76)	99.92(0.01)	99.43(0.11)	99.83(0.09)	99.75(0.13)	99.58(0.21)
6	325	83.61(5.98)	94.79(1.62)	93.9(2.46)	87.46(4.53)	96.95(3.33)	96.47(1.84)	98.57(2.11)	97.63(3.63)	89.82(2.21)	98.57(1.53)	96.73(2.34)
7	1208	75.28(8.21)	86.3(5.16)	89.98(2.48)	92.57(3.56)	89.82(4.28)	91.44(3.42)	91.99(2.59)	91.78(1.46)	83.09(4.52)	89.53(3.11)	95.73(1.76)
8	1244	66.23(2.54)	69.53(3.28)	76.94(2.88)	65.32(1.98)	79.00(3.07)	87.69(2.52)	89.07(1.62)	79.98(4.15)	81.32(6.62)	83.93(5.59)	80.57(5.17)
9	1252	69.93(3.37)	74.92(1.54)	86.82(3.22)	78.31(4.76)	84.62(3.53)	87.44(1.86)	79.70(5.43)	87.07(3.11)	83.03(6.57)	88.42(8.7)	82.21(4.03)
10	1227	71.2(6.82)	77.63(4.65)	87.13(2.58)	89.72(1.97)	93.98(2.25)	92.66(1.37)	92.05(0.58)	84.96(1.67)	91.33(1.88)	91.12(0.84)	93.29(1.21)
11	1235	84.67(2.43)	85.6(2.79)	89.21(0.86)	95.44(1.07)	94.85(2.47)	88.35(3.14)	95.38(1.19)	86.56(4.27)	85.23(3.53)	90.76(2.45)	96.46(0.75)
12	1233	92.69(1.45)	86.56(3.57)	87.63(3.15)	95.18(1.77)	83.62(5.52)	91.77(2.93)	92.85(0.84)	88.2(2.28)	89.94(1.86)	91.14(4.27)	94.84(1.01)
13	469	86.78(3.49)	90.87(2.46)	87.47(2.59)	89.98(1.76)	93.17(1.15)	89.46(5.34)	91.04(2.17)	91.57(2.49)	88.31(4.43)	91.98(2.14)	90.69(3.46)
14	428	98.06(1.02)	98.77(1.31)	99.25(0.21)	99.75(0.37)	96.73(1.14)	97.67(1.83)	96.08(2.15)	97.74(1.87)	100.0(0.0)	97.65(1.28)	98.94(0.82)
15	660	90.08(1.13)	98.75(1.28)	98.16(0.87)	99.84(0.23)	98.25(0.86)	97.41(1.34)	99.51(0.11)	98.57(1.12)	99.02(0.57)	98.86(0.75)	99.18(0.48)
OA ::		83.89(1.09)	88.34(1.54)	90.97(0.87)	91.24(0.72)	92.13(0.81)	93.06(1.53)	93.84(1.09)	91.72(0.76)	91.38(0.58)	92.48(1.21)	94.17(0.88)
AA ::		85.02(1.24)	89.88(0.67)	91.78(0.24)	91.89(1.15)	93.6(0.48)	93.6(1.15)	94.44(0.46)	92.68(0.41)	92.04(0.78)	93.41(0.98)	94.68(0.57)
Kappa ::		82.59(0.94)	87.41(0.1)	90.23(0.38)	90.53(0.84)	91.49(0.69)	92.49(2.07)	93.34(0.81)	91.65(0.67)	90.68(0.71)	91.87(1.53)	93.69(0.54)
Time (sec) ::		48.56	57.63	55.73	42.17	51.58	49.78	68.21	434.17	458.32	237.42	314.62

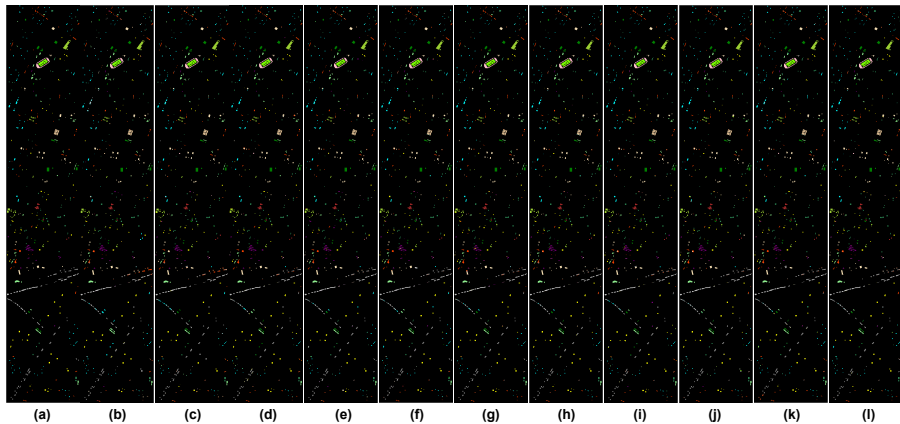


Fig. 14 (a) Ground Truth Image, Classification Maps of (b) SVM (c) EMP (d) EPF (e) SLIC (f) SCMK (g) SuperPCA (h) ASGSSK (i) CNN-PPF (j) 3D-CNN (k) Gabor-SLIC (l) LBP-SLIC for Houston 2013 dataset

5.3.4 Houston 2018

The quantitative results for Houston 2018 dataset with 0.2% training samples from each class are presented in Table 5. The corresponding classification map is shown in Figure. 15. As observed from Table 5, that the proposed methods are robust enough and achieve good classification results even for challenging scenes. The proposed approach improves the accuracy from 68.29 % to 82.56 % for the SVM method. The deep learning methods fail to improve the classifier accuracy in the presence of limited training samples. But, the superpixel based methods mainly ASGSSK approach significantly improves the classifier performance as the spatial contextual features are accurately incorporated using superpixels. Figure. 15 also highlights the superiority of the proposed method. The salt and pepper noise is reduced by a greater extent and a smoother classification map is produced with the proposed method.

Table 5 Classification Result for Houston 2018 Dataset with 0.2% training samples from each class for SVM, EMP, EPF, SLIC, SCMK, SuperPCA, ASGSSK, CNN-PPF, 3D-CNN, Gabor-SLIC, and LBP-SLIC algorithms. Number in the parentheses denote the standard deviation of the accuracies obtained in repeated experiments.

Class	Samples	SVM [32]	EMP [1]	EPF [33]	SLIC [28]	SCMK [21]	SuperPCA [34]	ASGSSK [35]	CNN-PPF [36]	3D-CNN [37]	Gabor-SLIC	LBP-SLIC
1	9799	64.07(11.21)	73.29(3.45)	65.71(6.2)	70.43(12.3)	70.31(4.28)	79.44(3.88)	76.81(10.2)	72.89(10.22)	77.34(8.36)	84.66(4.12)	84.09(2.25)
2	35202	81.5(0.89)	82.91(2.5)	85.08(1.45)	82.91(0.81)	86.83(1.67)	85.61(0.49)	89.22(4.21)	86.22(0.03)	86.09(2.71)	88.8(6.87)	90.55(1.22)
3	684	100.00(0.19)	100(0.00)	98.83(1.21)	100(0.00)	98.67(1.02)	98.23(1.92)	100(0.00)	99.56(0.51)	99.26(0.86)	83.6(5.58)	98.53(0.78)
4	13588	78.97(4.59)	74.04(6.26)	73.99(4.29)	78.04(13.12)	84.77(8.39)	86.91(12.1)	85.61(8.82)	82.06(8.87)	80.64(5.76)	91.41(2.17)	91.15(4.63)
5	5048	88.26(13.24)	41.89(8.66)	36.75(5.37)	46.84(7.26)	44.61(6.17)	53.97(3.88)	68.75(8.76)	50.00(1.67)	53.53(10.22)	40.98(12.31)	51.14(10.34)
6	4516	75.33(8.89)	87.19(4.47)	82.67(5.69)	82.47(5.73)	88.61(4.18)	85.79(1.82)	94.51(0.87)	88.91(3.56)	92.15(3.97)	78.03(5.41)	79.61(1.38)
7	266	15.09(5.23)	61.89(0.65)	67.80(8.89)	66.67(1.11)	68.18(3.14)	71.86(2.54)	86.59(8.1)	18.56(6.68)	14.77(7.13)	44.49(2.09)	74.71(11.57)
8	39762	72.37(2.98)	74.83(1.59)	77.29(3.62)	76.86(4.27)	78.48(3.08)	80.21(0.77)	85.24(1.54)	78.86(3.39)	77.99(2.56)	84.14(0.84)	85.77(5.15)
9	223684	83.42(0.54)	84.43(1.13)	85.51(0.85)	87.21(2.04)	87.11(0.67)	88.84(1.34)	91.76(0.17)	88.15(1.43)	87.64(0.62)	95.14(0.81)	95.98(0.16)
10	45810	35.41(2.23)	41.71(4.37)	43.73(14.4)	45.5(4.13)	45.42(3.48)	50.13(2.75)	57.63(2.67)	49.35(1.39)	46.10(5.31)	47.06(2.34)	56.84(3.45)
11	34002	33.69(5.07)	34.84(3.73)	35.3(2.82)	34.65(3.22)	34.1(2.07)	39.03(1.16)	45.31(3.48)	36.59(1.77)	35.81(0.59)	41.9(2.58)	46.79(5.31)
12	1516	10.19(0.21)	5.71(1.15)	9.02(6.81)	4.78(8.17)	6.3(3.86)	13.27(0.51)	12.18(7.79)	9.18(2.25)	8.57(1.35)	5.1(4.62)	2.69(6.13)
13	46358	51.73(9.37)	53.77(4.33)	55.91(4.98)	60.8(1.2)	60.74(6.52)	63.01(4.83)	71.63(1.16)	61.49(2.37)	62.38(3.62)	68.92(8.84)	71.26(5.28)
14	9849	55.81(8.64)	57.86(7.82)	60.35(3.65)	67.08(0.93)	64.68(11.32)	65.7(3.56)	75.6(1.1)	65.71(3.63)	61.24(10.12)	59.54(8.34)	67.79(6.18)
15	6937	72(5.22)	78.06(1.77)	85.83(2.61)	81.15(3.68)	82.05(5.63)	93.51(1.16)	96.59(0.65)	90.32(2.63)	92.06(5.04)	90.55(3.48)	91.87(7.31)
16	11475	60(3.48)	63.51(2.41)	63.2(2.53)	75.48(4.52)	69.41(8.18)	77.66(2.94)	82.14(3.74)	73.15(7.79)	66.28(7.35)	69.36(6.66)	71.12(4.14)
17	149	55.98(15.21)	63.51(5.28)	83.11(6.48)	37.84(15.61)	85.14(7.65)	76.87(2.27)	81.51(4.82)	80.7(4.73)	72.45(18.72)	22.45(18.72)	33.56(14.24)
18	6578	48.3(8.85)	40.84(7.05)	47(7.15)	44.97(6.89)	51.64(3.46)	61.35(1.48)	62.05(3.18)	58.19(8.83)	53.83(7.37)	63.35(6.84)	61.91(9.57)
19	5365	39.2(10.51)	48.52(7.56)	40.54(5.34)	45.36(6.24)	56.48(2.86)	63.29(12.94)	78.7(8.67)	57.61(5.36)	51.85(5.54)	42.15(7.19)	61.46(4.82)
20	6824	77.34(4.75)	83.27(5.58)	93.25(2.62)	90.57(3.47)	86.22(5.42)	96.43(0.78)	96.68(0.42)	94.11(1.06)	86.93(3.12)	81.44(7.58)	84.2(6.28)
OA ::		68.29(0.81)	70.39(0.51)	71.64(0.72)	73.46(0.48)	73.89(0.31)	76.7(0.62)	81.17(0.96)	75.49(1.06)	74.48(0.94)	79.62(0.38)	82.56(0.56)
AA ::		62.57(1.68)	62.77(1.23)	65.61(1.75)	64.05(1.15)	67.49(2.34)	71.56(1.45)	76.9(1.45)	64.78(1.02)	66.11(0.98)	64.13(1.44)	70.2(2.21)
Kappa ::		59.08(1.21)	61.77(0.52)	63.41(0.91)	65.62(0.65)	66.21(0.61)	69.93(0.82)	75.61(0.31)	68.26(0.64)	67.01(1.1)	72.94(1.51)	76.92(0.84)
Time (sec) ::		635.621	6528.6681	3957.48	1078.37	4978.61	1254.28	5629.37	9147.32	8762.41	7332.1	6937.71

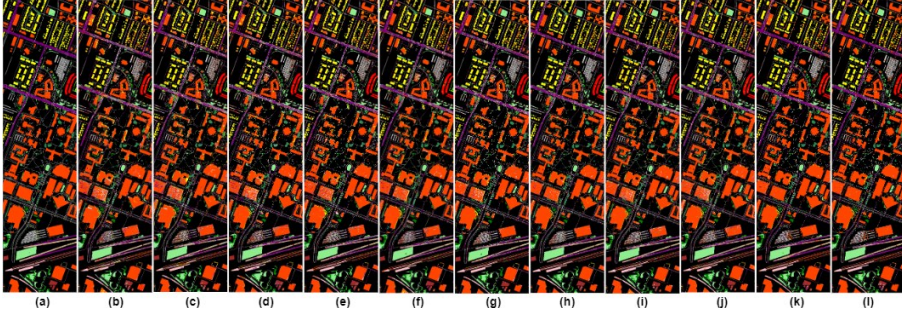


Fig. 15 (a) Ground Truth Image, Classification Maps of (b) SVM (c) EMP (d) EPF (e) SLIC (f) SCMk (g) SuperPCA (h) ASGSSK (i) CNN-PPF (j) 3D-CNN (k) Gabor-SLIC (l) LBP-SLIC for Houston 2018 dataset

The computation time for proposed method and the compared approaches for the four datasets are also presented in Tables. 2-5. It can be clearly observed that the computational cost of the proposed method is higher than most of the compared methods. However, the best classification result is provided by the proposed method at the expense of higher computational cost.

5.4 Statistical Evaluation

The effectiveness of the proposed method was statistically evaluated using the McNemar's test. The classification results for all the test cases are compared using this test. McNemar's test is defined as in Eqn. 13.

$$Z = \frac{f_{12} - f_{21}}{\sqrt{f_{12} + f_{21}}} \quad (13)$$

where, f_{12} indicates the number of samples correctly classified by Algorithm 1 and incorrectly classified by Algorithm 2. The performance of Algorithm 1 is better than Algorithm 2 if $Z > 0$. The difference between Algorithm 1 and 2 are statistically significant if $Z > 1.96$. McNemar's test between the proposed LBP-SLIC algorithm and other compared algorithms for Indian Pines, Pavia University, Houston 2013, and Houston 2018 dataset are provided in Table 6. The test result clearly reveals that classification result for the proposed method is statistically significant than other approaches.

6 Conclusion

The prime inspiration driving this work is to build up a superpixel segmentation framework for the accurate classification of HSI. Superpixels create semantic sub-regions from the image. So, instead of operating on individual pixels, classification is performed on more meaningful sub-regions. In this work, texture-based superpixel segmentation algorithms are proposed for the HSI image. Texture features like LBP and Gabor features are utilized for the construction of superpixels using SLIC. Several modifications were made in the

Table 6 Statistics of McNemar Test for Indian Pines, Pavia University, Houston 2013, and Houston 2018 dataset

z	IP	PU	Houston 2013	Houston 2018	IP	PU	Houston 2013	Houston 2018
	Proposed Method (Gabor-SLIC)				Proposed Method (LBP-SLIC)			
SVM	28.421	54.321	21.548	49.342	37.548	65.642	24.328	72.312
EMP	25.324	49.821	17.682	43.467	32.714	51.432	19.954	65.248
EPF	19.532	37.354	15.932	41.219	29.143	45.423	17.782	61.372
SLIC	12.278	34.439	9.197	38.334	16.753	36.214	13.457	55.225
SC-MK	15.351	22.649	10.216	35.614	18.783	34.294	11.423	51.673
SuperPCA	11.678	21.782	8.672	15.154	15.647	27.649	9.845	29.867
ASGSSK	8.345	11.649	6.792	13.534	13.045	24.314	8.237	18.431
CNN-PPF	5.732	17.354	7.321	28.624	11.468	19.971	7.114	32.614
3D-CNN	7.324	19.723	8.631	30.627	9.379	15.367	4.982	46.342

SLIC algorithm before utilizing the texture features as input. Some of the key changes are: the utilization of hexagonal grid structure for cluster initialization, and introduction of SID distance measure for accurate feature distance measurement. Later a majority voting strategy was carried out between the obtained superpixel map and pixel-wise classification map to produce the final classification map. The obtained results reveal the supremacy of the proposed LBP-SLIC approach against other state-of-the-art segmentation techniques.

Declarations

- **Funding:** This research received no external funding.
- **Conflict of interest:** The authors declare no conflict of interest.
- **Availability of data and materials:** Publicly available datasets have been utilized for conducting the experiments. Details are provided in the text of the paper.
- **Authors' contributions:** Conceptualization: [Subhashree Subudhi and Pradyut Kumar Biswal]; Methodology: [Subhashree Subudhi and Ramnarayan Patro]; Formal analysis and investigation: [Subhashree Subudhi and Ramnarayan Patro]; Writing - original draft preparation: [Subhashree Subudhi]; Writing - review and editing: [Subhashree Subudhi, Ramnarayan Patro and Pradyut Kumar Biswal]; Supervision: [Pradyut Kumar Biswal].

References

- [1] Benediktsson, J.A., Palmason, J.A., Sveinsson, J.R.: Classification of hyperspectral data from urban areas based on extended morphological profiles. *IEEE Transactions on Geoscience and Remote Sensing* **43**(3), 480–491 (2005)
- [2] Dalla Mura, M., Benediktsson, J.A., Waske, B., Bruzzone, L.: Morphological attribute profiles for the analysis of very high resolution images. *IEEE Transactions on Geoscience and Remote Sensing* **48**(10), 3747–3762 (2010)

- [3] Ghamisi, P., Dalla Mura, M., Benediktsson, J.A.: A survey on spectral–spatial classification techniques based on attribute profiles. *IEEE Transactions on Geoscience and Remote Sensing* **53**(5), 2335–2353 (2015)
- [4] Guo, X., Huang, X., Zhang, L.: Three-dimensional wavelet texture feature extraction and classification for multi/hyperspectral imagery. *IEEE Geoscience and remote sensing letters* **11**(12), 2183–2187 (2014)
- [5] Huang, X., Liu, X., Zhang, L.: A multichannel gray level co-occurrence matrix for multi/hyperspectral image texture representation. *Remote Sensing* **6**(9), 8424–8445 (2014)
- [6] Ye, Z., Fowler, J.E., Bai, L.: Spatial–spectral hyperspectral classification using local binary patterns and markov random fields. *Journal of Applied Remote Sensing* **11**(3), 035002 (2017)
- [7] Jia, S., Shen, L., Li, Q.: Gabor feature-based collaborative representation for hyperspectral imagery classification. *IEEE Transactions on Geoscience and Remote Sensing* **53**(2), 1118–1129 (2015)
- [8] Yang, J., Fan, J., Ai, D., Wang, X., Zheng, Y., Tang, S., Wang, Y.: Local statistics and non-local mean filter for speckle noise reduction in medical ultrasound image. *Neurocomputing* **195**, 88–95 (2016)
- [9] Kang, X., Li, S., Benediktsson, J.A.: Feature extraction of hyperspectral images with image fusion and recursive filtering. *IEEE Transactions on Geoscience and Remote Sensing* **52**(6), 3742–3752 (2014)
- [10] Tomasi, C., Manduchi, R.: Bilateral filtering for gray and color images. In: *Computer Vision, 1998. Sixth International Conference On*, pp. 839–846 (1998). IEEE
- [11] Kang, X., Li, S., Benediktsson, J.A.: Spectral–spatial hyperspectral image classification with edge-preserving filtering. *IEEE transactions on geoscience and remote sensing* **52**(5), 2666–2677 (2014)
- [12] Sun, W., Messinger, D.W.: Trilateral filter on multispectral imagery for classification and segmentation. In: *Algorithms and Technologies for Multispectral, Hyperspectral, and Ultraspectral Imagery XVII*, vol. 8048, p. 80480 (2011). International Society for Optics and Photonics
- [13] Vantaram, S.R., Piramanayagam, S., Saber, E., Messinger, D.: Spatial segmentation of multi/hyperspectral imagery by fusion of spectral-gradient-textural attributes. *Journal of Applied Remote Sensing* **9**(1), 095086 (2015)

- [14] Stutz, D., Hermans, A., Leibe, B.: Superpixels: An evaluation of the state-of-the-art. *Computer Vision and Image Understanding* **166**, 1–27 (2018)
- [15] Subudhi, S., Patro, R.N., Biswal, P.K., Dell’Acqua, F.: A survey on superpixel segmentation as a preprocessing step in hyperspectral image analysis. *IEEE Journal of Selected Topics in Applied Earth Observations and Remote Sensing* **14**, 5015–5035 (2021)
- [16] Ren, X., Malik, J.: Learning a classification model for segmentation. In: *Null*, p. 10 (2003). IEEE
- [17] Machairas, V., Decencière, E., Walter, T.: Waterpixels: Superpixels based on the watershed transformation. In: *2014 IEEE International Conference on Image Processing (ICIP)*, pp. 4343–4347 (2014). IEEE
- [18] Chen, Z., Wang, B.: An improved spectral-spatial classification framework for hyperspectral remote sensing images. In: *2014 International Conference on Audio, Language and Image Processing*, pp. 532–536 (2014). IEEE
- [19] Jiménez, L.I., Plaza, A., Ayma, V.A., Achanccaray, P., Costa, G.A., Feitosa, R.Q.: Segmentation as postprocessing for hyperspectral image classification. In: *IEEE EUROCON 2015-International Conference on Computer as a Tool (EUROCON)*, pp. 1–4 (2015). IEEE
- [20] Li, S., Jia, X., Zhang, B.: Superpixel-based markov random field for classification of hyperspectral images. In: *2013 IEEE International Geoscience and Remote Sensing Symposium-IGARSS*, pp. 3491–3494 (2013). IEEE
- [21] Fang, L., Li, S., Duan, W., Ren, J., Benediktsson, J.A.: Classification of hyperspectral images by exploiting spectral–spatial information of superpixel via multiple kernels. *IEEE transactions on geoscience and remote sensing* **53**(12), 6663–6674 (2015)
- [22] Yu, H., Gao, L., Liao, W., Zhang, B., Pižurica, A., Philips, W.: Multiscale superpixel-level subspace-based support vector machines for hyperspectral image classification. *IEEE Geoscience and Remote Sensing Letters* **14**(11), 2142–2146 (2017)
- [23] Tu, B., Yang, X., Li, N., Ou, X., He, W.: Hyperspectral image classification via superpixel correlation coefficient representation. *IEEE Journal of Selected Topics in Applied Earth Observations and Remote Sensing* **11**(11), 4113–4127 (2018)
- [24] Liu, T., Gu, Y., Chanussot, J., Dalla Mura, M.: Multimorphological superpixel model for hyperspectral image classification. *IEEE Transactions on Geoscience and Remote Sensing* **55**(12), 6950–6963 (2017)

- [25] Tang, X., Chen, J., Liu, Y., Sun, Q.-s.: Hyperspectral image classification by fusing sparse representation and simple linear iterative clustering. *Journal of Applied Remote Sensing* **9**(1), 095977 (2015)
- [26] Zhang, G., Jia, X., Hu, J.: Superpixel-based graphical model for remote sensing image mapping. *IEEE Transactions on Geoscience and Remote Sensing* **53**(11), 5861–5871 (2015)
- [27] Tarabalka, Y., Chanussot, J., Benediktsson, J.A.: Segmentation and classification of hyperspectral images using watershed transformation. *Pattern Recognition* **43**(7), 2367–2379 (2010)
- [28] Achanta, R., Shaji, A., Smith, K., Lucchi, A., Fua, P., Süsstrunk, S.: Slic superpixels compared to state-of-the-art superpixel methods. *IEEE transactions on pattern analysis and machine intelligence* **34**(11), 2274–2282 (2012)
- [29] Jia, S., Wu, K., Zhu, J., Jia, X.: Spectral–spatial gabor surface feature fusion approach for hyperspectral imagery classification. *IEEE Transactions on Geoscience and Remote Sensing* **57**(2), 1142–1154 (2018)
- [30] Chang, C.-I.: An information-theoretic approach to spectral variability, similarity, and discrimination for hyperspectral image analysis. *IEEE Transactions on information theory* **46**(5), 1927–1932 (2000)
- [31] Li, W., Chen, C., Su, H., Du, Q.: Local binary patterns and extreme learning machine for hyperspectral imagery classification. *IEEE Trans. Geoscience and Remote Sensing* **53**(7), 3681–3693 (2015)
- [32] Melgani, F., Bruzzone, L.: Classification of hyperspectral remote sensing images with support vector machines. *IEEE Transactions on geoscience and remote sensing* **42**(8), 1778–1790 (2004)
- [33] Kang, X., Li, S., Benediktsson, J.A.: Spectral–spatial hyperspectral image classification with edge-preserving filtering. *IEEE transactions on geoscience and remote sensing* **52**(5), 2666–2677 (2013)
- [34] Jiang, J., Ma, J., Chen, C., Wang, Z., Cai, Z., Wang, L.: Superpca: A superpixelwise pca approach for unsupervised feature extraction of hyperspectral imagery. *IEEE Transactions on Geoscience and Remote Sensing* **56**(8), 4581–4593 (2018)
- [35] Sun, L., Ma, C., Chen, Y., Shim, H.J., Wu, Z., Jeon, B.: Adjacent superpixel-based multiscale spatial-spectral kernel for hyperspectral classification. *IEEE Journal of Selected Topics in Applied Earth Observations and Remote Sensing* **12**(6), 1905–1919 (2019)

- [36] Li, W., Wu, G., Zhang, F., Du, Q.: Hyperspectral image classification using deep pixel-pair features. *IEEE Transactions on Geoscience and Remote Sensing* **55**(2), 844–853 (2016)
- [37] Chen, Y., Jiang, H., Li, C., Jia, X., Ghamisi, P.: Deep feature extraction and classification of hyperspectral images based on convolutional neural networks. *IEEE Transactions on Geoscience and Remote Sensing* **54**(10), 6232–6251 (2016)